Thermal design and simulation of mini-channel cold plate for water cooled large sized prismatic Lithium-ion battery

S. Panchal*[1], R. Khasow[2], I. Dincer[2], M. Agelin-Chaab[2], R. Fraser[1], and M. Fowler[3]

[1] Mechanical and Mechatronic Engineering Department, University of Waterloo, 200 University Avenue West, Waterloo, Ontario, Canada, N2L 3G1

[2] Department of Automotive, Mechanical & Manufacturing Engineering, Faculty of Engineering & Applied Science, University of Ontario Institute of Technology, 2000 Simcoe Street North, Oshawa, Ontario, Canada, L1H 7K4

[3] Chemical Engineering Departments, University of Waterloo, 200 University Avenue West, Waterloo, Ontario, Canada, N2L 3G1

*Corresponding Author's Telephone: +1-519-722-4420,

*Corresponding Author's Email: satyam.panchal@uwaterloo.ca

Abstract

This paper has presented a comparative study of the temperature and velocity distributions within the mini-channel cold plates placed on a prismatic lithium-ion battery cell using experimental and numerical techniques. The study was conducted for water cooling methods at 1C and 2C discharge rates and different operating temperatures of 5°C, 15°C, and 25°C. A total of nineteen thermocouples were used for this experimental work, and were purposefully placed at different locations. Ten T-type thermocouples were placed along the principal surface of the battery, and four K-type thermocouples were used to measure water inlet and outlet temperature. Computationally, the k-ε model in ANSYS Fluent was used to simulate the flow in a mini-channel cold plate, and the data was validated with the experimental data for temperature profiles. The present results show that increased discharge rates and increased operating temperature results in increased temperature of the cold plates. Furthermore, the sensors nearest the electrodes (anode and cathode) measured the higher temperatures than the sensors located at the center of the battery surface.

Keywords: Heat transfer, thermal analysis; Lithium-ion battery; mini-channel cold plate; battery thermal management; CFD.

1. Introduction

To alleviate the environment issues, the automotive industry has been forced to move towards sustainable vehicles such as electric vehicles (EVs), hybrid electric vehicles (HEVs), plug-in hybrid electric vehicles (PHEVs), and fuel cell vehicles (FCVs). In present days, lithium-ion batteries are the most cutting-edge battery technology used in the production of EVs, HEVs, and PHEVs [1]. Their broad usage is due to: 1) high specific energy and power densities [2, 3]; 2) high nominal voltage and low self-discharge rate [4]; and 3) long cycle-life and no memory effect [5]. To prolong the life of batteries, precautions must be

taken during discharging and charging since, for example exceeding the voltage, current or power limits may result in battery cell damage. The possibility of thermal runaways also occurs if care is not properly taken [6, 7]. Moreover, lithium-ion polymer batteries must be carefully monitored and managed (electrically and thermally) to avoid safety and performance related issues [8, 9, 10, 11].

The optimal operation of lithium-ion batteries, in terms of both efficiency and cycling life, depends critically on their thermal management [12, 13]. A battery thermal management system (BTMS) is required in order to secure the desired performance of a battery or battery pack in a low-temperature environment and the desired lifetime in a high-temperature environment [14, 15, 16]. In addition, the temperature, which is an important factor, affects several aspects of a lithium-ion battery, including the thermal and electrochemical behaviors, and ultimately performance and the cycle life cost [17, 18, 19]. A usual range of temperature is between 20°C and 40°C [20], and a prolonged range becomes between –10°C and +50°C for the allowable operation [21, 22] for lithium-ion batteries. There are different methods of BTMS that include: i) air cooling, ii) water cooling, and iii) phase change materials (PCM). The air cooling has attracted the attention of many researchers because of its simplicity [23] and light weight. The water cooling is more efficient method because of its ability to absorb more heat, as compared to air cooling, and it occupies less volume, but brings more complexities as well as high cost and weight [24, 25, 26]. In addition, because of the low thermal conductivity of air [27], higher air velocity is required to provide sufficient cooling effect of lithium-ion batteries using active cooling methods [28, 29]. On the other hand, liquid cooling gives better cooling as compared to the air cooling due to their high thermal conductivities [30]. The example of a passive system is a PCM. In a passive system, the ambient air is used to carry the heat rejected by cells. The effective passive design avoids the use of components like fans, manifold etc. [31, 32].

In this research, the flow inside the cold plates is turbulent and therefore for turbulence model in ANSYS Fluent is used. The Reynolds number is used to determine the flow regime (laminar or turbulent) and was defined as shown in Eq. 1.

$$R_e = \frac{v_s L}{\nu} \tag{1}$$

where, v_s is the mean fluid velocity (m/s), L is the characteristic dimension (m), ν is the kinematic fluid viscosity (m^2/s), also defined as μ/ρ, and ρ is the fluid density (kg/m^3). In this study, R_e = 8.7 x 10^3 and therefore the flow is considered turbulent.

The Reynolds-Averaged Navier-Stokes (RANS) based modeling approach, which averages the flow quantities for an entire range of scales of the turbulence being modeled, was employed. Two main RANS based turbulence models are available in Fluent: (1) K-Epsilon and (2) K-Omega.

The K-Epsilon model is the most broadly utilized turbulence models as it gives robustness, and simplicity. The main variations of the k- ϵ model available in Fluent include the standard k- ϵ, realizable and RNG (renormalization group) models The principle contrasts between the three models are as per the following: 1) the turbulent Prandtl numbers representing the turbulent diffusion of k and ϵ, 2) the generation and destruction terms in the equation for ϵ, and 3) the technique of calculating turbulent viscosity.

The K-Omega turbulence model also has two variations: the standard K-Omega model, and the shear stress transport (SST) model developed by Menter [33]. Both of these models use the same transport equations for k-ε . However, the SST model varies from the standard model as follows: 1) there is a slow change in the inner region of the boundary layer to the outer part of the boundary layer from the standard k-omega model to the k-epsilon model, and 2) the transport effects of the principal turbulent shear stress the SST model includes a modified turbulent viscosity equation.

There are different papers in the open literature for battery thermal modeling, utilizing CFD models [34, 35, 36, 17, 26, 37].

For example, Jarrett et al. [38] designed and modeled a battery cooling plate using CFD. Basically, a liquid cooling system model employed a serpentine channel and used CFD simulation to optimize the model. It was based on weighted average pressure drop, and the mean and standard deviation of the cold plate temperature. A numerical optimization was applied to improve its design. Their results indicate that a single design can satisfy both the average temperature and pressure objectives, but at the expense of temperature consistency.

Zhao et al. [39] proposed another cooling strategy for cylindrical batteries based on a mini-channel liquid cooled cylinder (LCC) to maintain the maximum temperature and local temperature difference within an appropriate range. The heat dissipation performance was numerically investigated by varying the effects of channel quantity, mass flow rate, flow direction and entrance size. Their outcome demonstrated that the most extreme temperature can be controlled under 40°C for 42,110 cylindrical batteries when the inlet mass flow rate is 1×10^{-3} kg/s and the number of mini-channels is also limited to four. They additionally found that the cooling style by a LCC can exhibit favorable circumstances contrasting the free convection cooling just when the channel number is higher than eight.

Saw et al. [40] considered CFD analysis in order to explore the air cooling method for a battery pack with 38,120 cells. With an accelerating rate calorimeter, they also measured the heat generated by the cell while charging. Utilizing steady state simulation, the thermal performances of the battery pack were analyzed with various mass flow rates of cooling air. The correlation between the Nusselt number and Reynolds number was derived from the numerical modeling results. Also, an experimental testing of the battery pack at different charging rates validated the correlation. Their strategy provided a basic approach to estimate the thermal performance of a battery pack when the battery pack is large and full transient simulation is not feasible.

In another study, Jin et al. [26] composed an oblique fin cold plate to cool down the batteries of an EV. In their outline, a basic configuration of oblique cuts across the straight fins of a conventional straight channel design was created, to enhance the performance of the conventional channel with minimal pressure penalty. These oblique cuts across the straight fins formed an oblique fin array. The composed liquid cold plate (LCP) contained these simple oblique fins with optimized angle and width. This segmentation of the continuous fin into oblique sections led to the re-initialization of boundary layers, giving an answer for the elevated temperatures caused by a thick boundary layer in the fully developed region. Their test results demonstrated that the heat transfer coefficients of an oblique mini-channel were higher than those of a conventional straight mini-channel. The oblique LCP can keep the battery surface average temperature below 50°C for 1240 W heat load at lower than 0.9 l/min flow rate.

Mohammadian et al. [41] reviewed internal and external cooling methods for thermal management of lithium-ion battery packs using 2D and 3D transient thermal analysis. For this, water and liquid electrolytes have been used as coolants for external and internal cooling, respectively. Their outcomes demonstrated that, at the same pumping power, utilizing internal cooling not only reduces the bulk temperature inside the battery more than external cooling, but also significantly decreases the standard deviation of the temperature field inside the battery. In conclusion, using internal cooling decreased the intersection angle between the velocity vector and the temperature gradient which, according to the field synergy principle (FSP), caused an increase the convection heat transfer.

Lastly, Huo et al. [42] similarly designed a battery thermal management system based on a mini-channel cold plate. Their design was to cool a rectangular lithium-ion battery. In their study, they developed a 3D thermal model of the cooling system and studied the effects of flow direction, inlet mass flow rate, number of channels and ambient temperature on temperature increase and distribution of the battery during the discharge process. The authors found that the most extreme temperature of the battery decreases with increases in the number of channels and the rate of inlet mass flow. They also concluded

that the effect of flow direction on cooling performance was smaller after mass flow rate increased, and that, with the increase of inlet mass flow rate, the cooling execution improved but the increasing trend became smaller, and the mass flow rate as 5×10^{-4} kg/s was optimal.

In this paper, a mini-channel cold plate based BTMS is designed for water cooling. A comprehensive investigation and simulation is conducted on the lithium-ion battery using the cold plate. From this the performance under different constant current discharge rates of 1C and 2C, and boundary conditions of 5°C, 15°C and 25°C are evaluated in detail.

2. Experimental Study

Here, the experimental details are provided through the experimental set-up, cold plate set-up along with battery, thermocouple locations, and experimental plan and procedure.

2.1 Experimental Set-up and Thermocouple Locations

The experimental set-up is shown in Figure 1 (a). Two commercial available cold plates are used for this experimental work to remove the heat generated from the lithium-ion battery during discharge. One cold plate is placed on the top surface of the battery and the other cold plate is placed on the bottom surface of the battery. A 20 Ah capacity lithium-ion pouch type battery cell is used for the test measurements and subsequent model validation. Table 1 tabulates the cell specifications. There are total 19 thermocouples employed for this experimental work. Out of 19, 10 T-type thermocouples are placed on the principle surface of the battery, which are shown in Figure 1 (b). 3 thermocouples are also pasted on the another surface of the battery, first near the cathode, second near the anode, and the third near the mid body. 2 thermocouples are used to measure the tab (electrode or current collector) temperature values during different discharge rates at various boundary conditions. Finally, 4 K-type thermocouples are used to measure water inlet and outlet temperature measurement for top and bottom cold plates.

2.2 Experimental Procedure

In the experimental work, three various coolant temperatures/operating temperatures are selected for the water cooling method: 5°C, 15°C, and 25°C. Two different discharge rates (constant current) are selected: 1C and 2C. The charge rate (constant current-constant voltage) is 1C. The experimental plan is shown in Table 2. The following procedure was performed: i) the isothermal water fluid bath and pump were turned on, two hours prior to beginning the cycling in order to bring the battery and cold plate set-up to a steady state temperature. The isothermal water fluid bath was set to the desired cooling temperature or BCs of 5 °C, 15 °C, and 25 °C for the test. ii) The LabVIEW for the charge/discharge of the battery

(battery electrical data collection) was started and the test parameters, such as charge current, discharge current, charge voltage, discharge voltage, and sampling rate were input to the program. iii) The thermal data acquisition PC (Computer-2) and Keithly 2700 were turned on and allowed to initialize. On the PC, data acquisition were performed such as surface temperature and water inlet and outlet temperature at the top and bottom of the cold plate.

2.3 Heat Generation in a Lithium-ion Battery

Understanding the rate of heat generation and dissipation inside the lithium-ion cell is important since the performance of lithium-ion battery strongly dependent on temperature. Heat generation inside the battery is a complex process and is dependent on the electrochemical reaction rates; it also changes with time and temperature. As shown in Figure 2, the active materials in both electrodes (positive and negative electrode) behave like an important element for the lithium content of the battery in a lithium-ion cell. The lithium-ions can be removed from or inserted into active material particles without significant change of the structure of the element. This process called exchange process is the basis of lithium-ion batteries. During the charging process, lithium-ion are removed from the active side in the positive electrode and inserted into the negative electrode [43, 44]. In Figure 2, $LiMO_2$ is a metal oxide material used in the positive electrode and C is a carbonaceous material used in the negative electrode. In the discharge process, lithium-ion travel through the electrolyte to positive electrode. The electrochemical reaction for positive electrode, for negative electrode, and the overall reaction is given by

Positive electrode : $$LiMO_2 \underset{Discharge}{\overset{Charge}{\longrightarrow}} Li_{1-x}MO_2 + x\ Li^+ + xe^- \quad (2)$$

Negative electrode : $$C + x\ Li^+ + xe^- + LiMO_2 \underset{Discharge}{\overset{Charge}{\longrightarrow}} Li_xC \quad (3)$$

Overall : $$LiMO_2 + C \underset{Discharge}{\overset{Charge}{\longrightarrow}} Li_xC + Li_{1-x}MO_2 \quad (4)$$

The heat generation in a battery cell has two primary sources: (i) change in entropy because of electrochemical reactions and (ii) Joule's heating or ohmic heating [45, 46, 47]. Based on the pair of electrodes, the reaction heat can be of two types; exothermic for discharging, and endothermic for charging. The Joule or Ohmic part of heating is because of the exchange of current at internal resistances [48]. The rate of heat generation can be computed as follows:

$$\dot{Q} = I(E - C) - I\left[T\left(\frac{dE}{dT}\right)\right] \tag{5}$$

where the primary term, $I\ (E - C)$ is the Joule or Ohmic heat generation and other irreversible effects in the battery cell. The secondary term, $I\ \left[T\left(\frac{dE}{dT}\right)\right]$ is the heat produced or expended in light of the reversible entropy change which is due to electrochemical reactions inside the battery cell. In practical HEV as well as EV current rates, the secondary term for the most part is negligible contrasted with the primary term [49]. Here, the rate of heat generation reformulated by Fathabadi [50] and is given by

$$\dot{Q} = I^2R - T\,\Delta S\,\left[\frac{I}{n\,F}\right] \tag{6}$$

where, I is the current and $I > 0$ for discharge, $I < 0$ for charge, (i.e. +Ve value is taken for discharging and –Ve value is taken for charging), R is the resistance, ΔS is the change in entropy, n is the number of flow of electron, and F is the Faraday's constant (96485 Columb/mol).

3. Numerical Modeling

3.1 Governing Equations

As mentioned earlier, the flow in this study is turbulent and therefore it is modeled by Reynolds-Averaged Navier-Stokes Equations (RANS). Although analytical solutions for these flows are not accurate, on the basis of the continuum fluid assumption, the dynamics of turbulence is adequately described by the continuity and Navier-Stokes equations. In this paper, the goal of this CFD study is to obtain trends that can be compared with the experimental measurements. In addition, because the experimental technique obtained only point-wise data the CFD technique provides the whole field and comprehensive data to complement the experimental data. Since the temperature field is also of interest, the energy equation is solved as well. The governing equations are:

$$\nabla * \bar{V} = 0 \tag{7}$$

$$\rho\left[\frac{\partial \bar{V}}{\partial t} + \left(\vec{V} \cdot \nabla \bar{V}\right)\right] = -\nabla \bar{p} + \left(\mu \nabla^2 \bar{V} - \lambda\right) \tag{8}$$

$$\frac{\partial \rho T}{\partial t} + \nabla * \left[\rho \vec{V} T\right] = \nabla * \left[\left(\frac{\mu}{Pr} + \frac{\mu_t}{Pr_t}\right)\nabla T\right] \tag{9}$$

Where, ∇ is the gradient operator, $\bar{V}$ is the average velocity (m/s), V is the speed (m/s), P is the pressure (Pa), λ is the Reynold's stress, Pr is the Prandtl number, and Pr_t is the turbulent Prandtl number.

Since the flow in the problem is assumed to be turbulent an appropriate turbulence model is required. In this study the standard *k-ε* turbulence model was used given the robustness of the model, reasonable accuracy for a wide range of flows and its proven capability in heat transfer and flow analysis. The equations in ANSYS Fluent for turbulent kinetic energy and eddy viscosity are as below [51]:

$$\frac{\partial \rho k}{\partial t} + \nabla * \left[\rho \overrightarrow{V} k\right] = \nabla * \left[\left(\mu + \frac{\mu_t}{\sigma_k}\right) \nabla k\right] + G_k + G_b - \rho\varepsilon - Y_M + S_k \tag{10}$$

$$\frac{\partial \rho \varepsilon}{\partial t} + \nabla * \left[\rho \overrightarrow{V} \varepsilon\right] = \nabla * \left[\left(\mu + \frac{\mu_t}{\varepsilon_k}\right) \nabla \varepsilon\right] + C_1 \frac{\varepsilon}{k}(G_k + C_3 G_b) - C_2\, \rho\, \frac{\varepsilon^2}{k} + S_\varepsilon \tag{11}$$

where C_1, C_2, C_3 are the model constants, σ_k and ε_k are the turbulent Prandtl numbers for k and ε. G_k represents the generation of turbulence kinetic energy due to the mean velocity gradients, G_b is the generation of turbulence kinetic energy due to buoyancy. Y_M represents the contribution of the fluctuating dilatation in compressible turbulence to the overall dissipation rate. S_k and S_ε are user-defined source terms. The turbulent (or eddy) viscosity is computed by combining k and ε as follows:

$$\mu_t = C_\mu\, \rho\, \frac{k^2}{\varepsilon} \tag{12}$$

where C_μ is a constant. As stated earlier the commercial CFD software ANSYS Fluent is used in this study because of its flexibility and availability. Starting from an initial condition the solution converges to a steady-state. Convergence is judged against the normalized continuity, momentum and energy residuals and is considered converged when these residuals reduce to 1×10^{-6}.

3.2 Geometry in NX 8.5 and Boundary Conditions

The full geometry with the top and bottom cold plates along with lithium-ion battery in NX 8.5 is depicted in Figure 3 (a and b). In a CFD simulation the term "wall" refers to any solid surface that the flow cannot penetrate and thus includes the walls, the floor, ceiling, and surfaces of the test battery. The following parameters are selected for the model development: 1) viscous model: R_e = 8.7 x 10^3, 2) the wall distance is 1.1 x 10^{-4}, 3) C_1= 1.44, 4) C_2 = 1.92, 5) TKE Prandtl number =1, 6) TDR Prandtl number =1.3, 7) energy Prandtl number =0.85, 8) wall Prandtl number =0.85, 9) in the Turbulent specification method: Turbulent intensity of 5%, and turbulent viscosity ratio of 10, 10) solver: type: pressure based,

time: steady state, velocity formulation: absolute velocity, 11) residuals convergence variables: X-velocity, Y-velocity, Z-velocity, energy, k-epsilon, continuity equation, 12) wall treatment (y^+=5), 13) number of elements: approximately 20 million, 14) method for meshing: unstructured tetrahedral with prism wall layers, 15) convergent criteria: 0.000001 residuals, 16) 1st or 2nd order: 2nd order, 17) type of flow: turbulent, 18) Prism meshing parameters: growth law: exponential, initial height: 0.1, height ration: 1.1, number of layers : 3, total height : 0.331, minimum prism quality : 0.009, ortho weight: 0.50, fillet ratio: 0.1, 17) global mesh size: global element scale factor: 1, global element seed size: 1, curvature/proximity based refinement minimum size limit: 1. Finally, it was assumed: 1) symmetry about center of battery, and 2) adiabatic on outside surface of cooling plate.

The flow is considered incompressible, steady state and turbulent. Water is chosen as the working fluid with a density of 998.2 kg/m^3 and dynamic viscosity of 1.002 x 10^{-3} N s/m^2. The computational grid consists of 20 million elements. A uniform free stream velocity inlet boundary condition for incompressible flow is applied upstream of the step. Average velocity is applied at the inlet using a derived relation valid for channel flows. The inlet and outlet boundary conditions were set based on the turbulent intensity and turbulent length scale. The turbulent intensity of 5% to be consistent with the value obtained by the experimental study is used. The velocity is 0.5784 m/s. The pressure outlet boundary condition was applied at the outflow plan which is positioned far downstream of the step to reduce the influence of the outflow conditions and on all other surfaces the no-slip boundary condition is applied. The enhanced wall treatment (y^+=1) as the near wall function applied.

3.3 Meshing

The meshing of the domain is a very important step since various meshing parameters, such as the number of nodes and the shape of the elements have a significant impact on the accuracy of the results and the numerical behavior of the solution. A fine unstructured tetrahedral mesh is generated using ANSYS ICEM to resolve all flow features of interest. The mesh resolution at various locations within the geometry is shown in Figure 4 (a and b). This meshing is at the inlet and the outlet channel of the cold plate's places on top and bottom of the lithium-ion battery cell. The overall meshing generated within the assembly is shown in Figure 5 (a and b). The flow along the various surfaces in the space is resolved by using a finer mesh size around those obstacles while the boundary layers along all surfaces are resolved by clustering 3 layers of prismatic elements near the walls. The prismatic layers are also adjusted such that the first node is 0.1 mm away from the wall. This wall node spacing yields a dimensionless wall distance of y^+ ~1, where y^+ is chosen to be 5. This value is consistent with the recommended value for near wall flows while being closer to acceptable values for the standard k-ε turbulence model. It trades off extreme resolution with lower y^+ values but still maintaining some approximation of the boundary layer.

Using recommended values of $y^+ \geq 30$ resulted in first layer thickness being larger than the channel height itself thus necessitating compromises. The total number of elements used for the mesh is approximately 20 million. It is ensured that the numerical results are mesh independent by conducting grid independence tests. Negligible effect in the reattachment points is observed for mesh elements greater than 10 million. It is assured that the numerical residuals are in the order of magnitude 10^{-6} and solution is considered converged as numerical residuals reached the convergence criteria. The solution did not change much after this criterion is achieved. The analysis is also performed at different planes in the channel. Figure 6 shows the vertical planes within the cold plates for CFD analysis, where 1 is inlet to the cold plate and 4 is the outlet from the cold plate.

4. Results and Discussion

This section explains the results obtained for a particular prismatic lithium-ion battery at different discharge rates of 1C and 2C for water-cooling at operating conditions of 5°C, 15°C, and 25°C.

4.1 Temperature and Velocity Contours at 1C and 5 °C, 15 °C, and 25 °C Operating Temperatures

The temperature contours obtained from CFD at 1C discharge rate and 5 °C, 15 °C, and 25 °C operating temperatures (water cooling) is shown in Figure 7 (a, b, and c). These contours are obtained at the midplane of the cooling plate. To remind readers, ten thermocouples are located on the principle surface of the battery: one is located near the positive electrode or cathode, the second is located near the negative electrode or anode, and the third is located at the middle of the cell (mid-body) along the height of the cell. That is, three are placed near electrodes, three are placed at the center of the battery, two are placed between the top and the middle of the battery, one is placed at the bottom of the battery and one is located between the center and the bottom of the battery. It is observed that there is a great impact of operating temperature on the performance of battery and cold plates and it is observed that as the operating temperature increases between 5 °C to 25 °C for a particular discharge rate of 1C, the temperature contour values are also increased. The general cooling patterns are the same, showing greater temperature differences at the inlet of the cooling plate when the water is coldest. The temperatures vary with the inlet temperature boundary condition, but the overall pattern remains roughly the same, with Figure 6 (a) being the exception. This is likely due to the low temperature differences involved. The cooling patterns follow what is seen on the batteries experimentally, with the outlet being higher temperature than the inlet. The velocity contours are identical in all the cases, this is expected, given the low temperatures involved in the simulations that would have little to no effect on the density of the water. These results may be affected by the low y^+ value, wall functions and turbulence model used. Table 3 provides the summary of water inlet and outlet temperature at 1C discharge rates and different operating temperatures of 5 °C, 15 °C, and

25 °C. The corresponding velocity contours at 1C discharge rate and 5 °C, 15 °C, and 25 °C operating temperatures appears in Figure 7 (d, e, and f).

4.2 Temperature and Velocity Contours at 2C and 5 °C, 15 °C, and 25 °C Operating Temperatures

The temperature contours at 2C discharge rate and 5 °C, 15 °C, and 25 °C operating temperatures are shown in Figure 8 (a, b, and c). It is observed that as the battery discharges the circulating water in the cold plates gets heated which is obvious. As the discharge rate increases from 1C to 2C, there is an increase in temperature values as well. The trend observed is that increased discharge rates and decreased BCs results in increased temperatures in the cold plate. Table 3 provides the summary of water inlet and outlet temperature at 2C discharge rates and different operating temperatures of 5 °C, 15 °C, and 25 °C. Again, the general cooling patterns are the same, similar to the results in Section 4.1. There are greater temperature differences at the inlet of the cooling plate when the water is coldest. The temperature values vary with the inlet temperature boundary condition, but the overall pattern remains roughly the same. Likewise, the velocity contours are the same in all the cases. Figure 8 (d, e, and f) shows the corresponding velocity contours at 2C discharge rate and 5 °C, 15 °C, and 25 °C operating temperatures.

Similarly, the temperature and velocity contours are also obtained at inlet and outlet plane (plane 1 and plane 4) of the mini-channel cold plate. Figure 9, Figure 10, and Figure 11 show the temperature and velocity contours at 2C discharge rate and 5°C, 15°C, and 25°C operating temperatures. In addition to this study, the effect of discharge rate on the performance of the battery is also studied and it is found that there is a great effect of both C-rate and the operating temperatures on the performance of the battery. At lower discharge rates, the battery capacity stays closer to the manufacturer's specifications, but as C-rate increases, there is a reduction in the discharge capacity. Even when the boundary conditions change from 25 °C to 5 °C, there is a greater reduction in the discharge capacity. Overall, it is noted that the increased C-rates and decreased boundary conditions resulting in the decrease discharge capacity.

5. Conclusions

This paper has presented a comparative study of the temperature and velocity distributions within the mini-channel cold plates placed on a prismatic lithium-ion battery cell using both experimentally and theoretically (through simulation methods by using ANSYS-RANS approach) for water cooling methods at 1C and 2C discharge rates and different operating temperatures of 5°C, 15°C, and 25°C. Some closing remarks are then stated as follows: (i) the temperature distributions within mini-channel cold plates increase as the C-rates increase; (ii) increasing discharge rates (between 1C and 2C) increased the temperatures measured at ten distributed locations on battery surface; and (iii) the thermocouple sensors

closest to the electrodes provide higher temperatures than the centerline-thermocouple sensors. The cooling patterns from the simulations are consistent with those obtained experimentally. These results provide insights into the design and optimization of battery systems.

Nomenclature

C	=	cell voltage or cell potential [V]
C_1	=	model constants
C_2	=	model constants
C_3	=	model constants
C_μ	=	constant
F	=	Faraday's constant (96485 Columb/mol)
G_k	=	generation of turbulence kinetic energy due to the mean velocity gradients
G_b	=	generation of turbulence kinetic energy due to buoyancy
I	=	current [A]
k	=	turbulent kinetic energy (J)
L	=	characteristic dimension (m)
n	=	number of flow of electron
P	=	pressure (Pa)
Pr	=	Prandtl number
$\dot{Q}$	=	heat generation rate [W]
R	=	resistance (Ω)
Re	=	Reynold's number
S_k	=	user-defined source terms
S_ε	=	user-defined source terms
ΔS	=	change in entropy (J/K)
T	=	temperature [°C or K]
t	=	time [s]
V	=	speed (m/s)
v_s	=	mean fluid velocity (m/s)
$\bar{V}$		average velocity (m/s)
dE/dT	=	temperature coefficient [V/°C]
ω	=	turbulent eddy frequency (1/s)
y^+	=	enhanced wall treatment

Y_M	=	the contribution of the fluctuating dilatation in compressible turbulence to the overall dissipation rate

Greek Symbols

∇	=	gradient operator
ρ	=	density (kg/m^3)
ν	=	kinematic fluid viscosity (m^2/s)
μ	=	dynamic fluid viscosity (Ns/m^2)
λ	=	Reynold's stress
σ_k	=	turbulent Prandtl numbers for k
ε_k	=	turbulent Prandtl numbers for ε

Subscripts

act	=	actual
chg	=	charge
dis	=	discharge
n	=	negative
p	=	positive
sim	=	simulated

Superscripts

°	=	degree
$^+$	=	Related to wall treatment

Acronyms

A	Ampere
Ah	Ampere-hour
ANSYS Inc.	American Computer-aided engineering software developer
ANSYS-CFX	A computation fluid dynamics software tools
BEV	Battery electric vehicle
BC	Boundary condition
BTMS	Battery thermal management system
C	Capacity
CFD	Computational fluid dynamics
EV	Electric vehicle
FCV	Fuel cell vehicle

FEM	Finite element method
FSP	Field synergy principle
HEV	Hybrid electric vehicle
ICEM-CFD	Popular proprietary software package used for CAD and mesh generation
LCC	Liquid cooled cylinder
LabVIEW	Laboratory virtual instrument engineering workbench
$LiMO_2$	Lithium manganese oxide
$LiFePO_4$	Lithium iron phosphate
LCC	Liquid cooled cylinder
LCP	Liquid cold plate
LPM	Lumped parameter model
LPV	Linear parameter varying
PC	Personal computer
PCM	Phase change material
PDE	Partial differential equation
PHEV	Plug-In hybrid electric vehicle
RNG	Renormalization group
RANS	Reynolds-Averaged Navier-Stokes
SST	Shear Stress Transport
TDR	Turbulent Dissipation Rate
TKE	Turbulent Kinetic Energy
2D	Two-dimensional
3D	Three-dimensional

References

[1] Q. Wang, Q. Sun, P. Ping, X. Zhao, J. Sun and Z. Lin, "Heat transfer in the dynamic cycling of lithium–titanate batteries," International Journal of Heat and Mass Transfer, no. 93, pp. 896-905, 2016.

[2] Z. Ling, F. Wang, X. Fang, X. Gao and Z. Zhang, "A hybrid thermal management system for lithium ion batteries combining phase change materials with forced-air cooling," Applied Energy, no. 148, pp. 403-409, 2015.

[3] H. Ge, J. Huang, J. Zhang and Z. Li, "Temperature-Adaptive Alternating Current Preheating of Lithium-Ion Batteries with Lithium Deposition Prevention," Journal of The Electrochemical Society,

vol. 163, no. 2, pp. A290-A299, 2016.

[4] A. Ritchie and W. Howard, "Recent developments and likely advances in lithium-ion batteries," Journal of Power Sources, vol. 162, pp. 809-812, 2006.

[5] Y. Ye, L. H. Saw, Y. Shi and A. A. Tay, "Numerical analyses on optimizing a heat pipe thermal management system for lithium-ion batteries during fast charging," Applied Thermal Engineering, vol. 86, pp. 281-291, 2015.

[6] M. J. Isaacson, R. P. Hollandsworth, P. J. Giampaoli, F. A. Linkowsky, A. Salim and V. L. Teofilo, "Advanced Lithium-ion battery charger," Battery conference on Applications and Advances, pp. 193-198, 2000.

[7] J. McDowall, P. Biensan and M. Broussely, "Industrial Lithium-ion battery safety-What are the tradeoffs?," in Telecommunications Energy Conference, 2007.

[8] Y. Xing, Q. Miao, K.-L. Tsui and M. Pecht, "Prognostics and health monitoring for lithium-ion battery," in IEEE International Conference on, 2011.

[9] X. Feng, M. Fang, X. He, M. Ouyang, L. Lu, H. Wang and M. Zhang, "Thermal runaway features of large format prismatic lithium ion battery using extended volume accelerating rate calorimetry," Journal of Power Sources, pp. 255 : 294-301, 2014.

[10] L. Lu, X. Han, J. Hua, M. Ouyang and J. Li, "A review on the key issues for lithium-ion battery management in electric vehicles," Journal of Power Sources, pp. 226:272-288, 2013.

[11] S. Panchal, I. Dincer, M. Agelin-Chaab, R. Fraser and M. Fowler, "Transient electrochemical heat transfer modeling and experimental validation of a large sized LiFePO4/graphite battery," International Journal of Heat and Mass Transfer, vol. 109, pp. 1239-1251, 2017.

[12] C. Alaoui, "Solid-State Thermal Management for Lithium-Ion EV Batteries," Vehicular Technology, IEEE Transactions on, vol. 62, no. 1, pp. 98-107, 2013.

[13] Z. Rao, Y. Huo and X. Liu, "Experimental study of an OHP-cooled thermal management system for electric vehicle power battery," Experimental Thermal and Fluid Science, vol. 57, pp. 20-26, 2014.

[14] S. Panchal, S. Mathewson, R. Fraser, R. Culham and M. Fowler, "Thermal Management of Lithium-Ion Pouch Cell with Indirect Liquid Cooling using Dual Cold Plates Approach," SAE International, vol. 4, no. 2, pp. 1-15, 2015.

[15] S. Panchal, I. Dincer, M. Agelin-Chaab, R. Fraser and M. Fowler, "Experimental and theoretical investigation of temperature distributions in a prismatic lithium-ion battery," International Journal of Thermal Sciences, vol. 99, pp. 204-212, 2016.

[16] S. Panchal, I. Dincer, M. Agelin-Chaab, R. Fraser and M. Fowler, "Thermal modeling and validation

of temperature distributions in a prismatic lithium-ion battery at different discharge rates and varying boundary conditions," Applied Thermal Engineering, vol. 96, pp. 190-199, 2016.

[17] C. H. Wang, T. Lin, J. T. Huang and Z. H. Rao, "Temperature response of a high power lithium-ion battery subjected to high current discharge," Materials Research Innovations, vol. 19, pp. 156-160, 2015.

[18] Z. Rao, S. Wang, M. Wu, Z. Lin and F. Li, "Experimental investigation on thermal management of electric vehicle battery with heat pipe," Energy Conversion and Management, vol. 65, pp. 92-97, 2013.

[19] S. Panchal, I. Dincer, M. Agelin-Chaab, M. Fowler and R. Fraser, "Uneven temperature and voltage distributions due to rapid discharge rates and different boundary conditions for series-connected LiFePO 4 batteries," International Communications in Heat and Mass Transfer, vol. 81, pp. 210-217, 2017.

[20] H. Teng, Y. Ma, K. Yeow and M. Thelliez, "An Analysis of a Lithium-ion Battery System with Indirect Air Cooling and Warm-Up," SAE International Journal of Passenger Cars- Mechanical Systems, vol. 4, no. 3, pp. 1343-1357, 2011.

[21] F. He and L. Ma, "Thermal Management in Hybrid Power Systems Using Cylindrical and Prismatic Battery Cells," Heat Transfer Engineering, vol. 37, no. 6, pp. 581-590, 2016.

[22] I. Bayraktar, "Computational Simulation Methods for Vehicle Thermal Management," Applied Thermal Engineering, vol. 36, pp. 325-329, 2012.

[23] M. R. Giuliano, A. K. Prasad and S. G. Advani, "Experimental study of an air-cooled thermal management system for high capacity lithium–titanate batteries," Journal of Power Sources, vol. 216, pp. 345-352, 2012.

[24] G.-H. Kim, A. Pesaran and R. Spotnitz, "A three-dimensional thermal abuse model for lithium-ion cells," Journal of Power Sources, vol. 170, no. 2, pp. 476-489, 2007.

[25] M. R. Giuliano, S. G. Advani and A. K. Prasad, "Thermal analysis and management of lithium–titanate batteries," Journal of Power Sources, vol. 196, no. 15, pp. 6517-6524, 2011.

[26] L. W. Jin, P. S. Lee, X. X. Kong, Y. Fan and S. K. Chou, "Ultra-thin minichannel LCP for EV battery thermal management," Applied Energy, vol. 113, pp. 1786-1794, 2014.

[27] E. W. Lemmon and R. T. Jacobsen, "Viscosity and Thermal Conductivity Equations for Nitrogen, Oxygen, Argon, and Air," International Journal of Thermophysics, vol. 25, no. 1, pp. 21-69, 2004.

[28] H. Park, "A design of air flow configuration for cooling lithium ion battery in hybrid electric vehicles," Journal of Power Sources, vol. 239, pp. 30-36, 2013.

[29] L. Fan, J. M. Khodadadi and A. A. Pesaran, "A parametric study on thermal management of an air-cooled lithium-ion battery module for plug-in hybrid electric vehicles," Journal of Power Sources, vol. 238, pp. 301-312, 2013.

[30] Z. Rao and S. Wang, "A review of power battery thermal energy management," Renewable and Sustainable Energy Reviews, vol. 15, no. 9, pp. 4554-4571, 2011.

[31] C. Lin, S. Xu, G. Chang and J. Liu, "Experiment and simulation of a LiFePO4 battery pack with a passive thermal management system using composite phase change material and graphite sheets," Journal of Power Sources, vol. 275, pp. 742-749, 2015.

[32] Q. Wang, B. Jiang, B. Li and Y. Yan, "A critical review of thermal management models and solutions of lithium-ion batteries for the development of pure electric vehicles," Renewable and Sustainable Energy Reviews, vol. 64, pp. 106-128, 2016.

[33] R. Khasow, "Aerodynamic and thermal analysis of a heat source at the underside of a passanger vehicle," University of Ontario Institute of Technology, Oshawa, 2016.

[34] A. Samba, N. Omar, H. Gualous, Y. Firouz, P. V. d. Bossche, J. V. Mierlo and T. I. Boubekeur, "Development of an advanced two-dimensional thermal model for large size lithium-ion pouch cells," Electrochimica Acta, vol. 117, pp. 246-254, 2014.

[35] G. Li and S. Li, "Physics-based CFD simulation of lithium-ion battery under the FUDS driving cycle," ECS Transactions, vol. 64, no. 33, pp. 1-14, 2015.

[36] P. Vyroubal, T. Kazda, J. Maxa and J. Vondrák, "Analysis of temperature field in lithium-ion battery by discharging," ECS Transactions, vol. 70, no. 1, pp. 269-273, 2015.

[37] K. Yeow, M. Thelliez, H. Teng and E. Tan, "Thermal analysis of a Li-ion battery system with indirect liquid cooling using finite element analysis approach," SAE International Journal, vol. 1, no. 1, pp. 65-78, 2012.

[38] A. Jarrett and I. Y. Kim, "Design optimization of electric vehicle battery cooling plates for thermal performance," Journal of Power Sources, vol. 196, no. 23, pp. 10359-10368, 2011.

[39] J. Zhao, Z. Rao and Y. Li, "Thermal performance of mini-channel liquid cooled cylinder based battery thermal management for cylindrical lithium-ion power battery," Energy Conversion and Management, vol. 103, pp. 157-165, 2015.

[40] L. H. Saw, Y. Ye, A. A. Tay, W. T. Chong, S. H. Kuan and M. C. Yew, "Computational fluid dynamic and thermal analysis of lithium-ion battery pack with air cooling," Applied Energy, vol. 177, pp. 783-792, 2016.

[41] S. Mohammadian, Y. L. He and Y. Zhang, "Internal cooling of a lithium-ion battery using electrolyte as coolant through microchannels embedded inside the electrodes," Journal of Power Sources, vol.

293, pp. 458-466, 2015.

[42] Y. Huo, Z. Rao, X. Liu and J. Zhao, "Investigation of power battery thermal management by using mini-channel cold plate," Energy Conversion and Management, vol. 89, pp. 387-395, 2015.

[43] S. Panchal, S. Mathewson, R. Fraser, R. Culham and M. Fowler, "Experimental Measurements of Thermal Characteristics of LiFePO4 Battery," SAE Technical Paper, Vols. doi:10.4271/2015-01-1189, pp. 1-11, 2015.

[44] S. Panchal, S. Mathewson, R. Fraser, R. Culham and M. Fowler, "Measurement of Temperature Gradient (dT/dy) and Temperature Response (dT/dt) of a Prismatic Lithium-Ion Pouch Cell with LiFePO4 Cathode Material," SAE International, Vols. doi:10.4271/2017-01-1207, pp. 1-9, 2017.

[45] C. R. Pals and J. Newman, "Thermal modeling of the lithium/polymer battery," Journal of the Electrochemical Society, vol. 142, no. 10, pp. 3274-3281, 1995.

[46] Y. Chen and J. W. Evans, "Three-dimensional thermal modeling of lithium-polymer batteries under galvanostatic discharge and dynamic power profile," Journal of the Electrochemical Society, vol. 141, no. 11, pp. 2947-2952, 1994.

[47] G. Wierschem, B. McKinney and E. Nrotek, "Thermal management of lead-acid batteries for electric vehicles," in Research and developement testing, Detroit, 1993.

[48] A. A. Pesaran, A. Vlahinos and S. D. Burch, "Thermal performance of EV and HEV battery modules and packs," National Renewable Energy Laboratory, Golden, Colorado, 1997.

[49] K. Smith and C.-Y. Wang, "Power and thermal characterization of a lithium-ion battery pack for hybrid-electric vehicles," Journal of Power Sources, vol. 160, no. 1, pp. 662-673, 2006.

[50] H. Fathabadi, "A novel design including cooling media for Lithium-ion batteries pack used in hybrid and electric vehicles," Journal of Power Sources, vol. 245, pp. 495-500, 2014.

[51] Inc., ANSYS, "ANSYS Fluent Advanced Add-On Modules," ANSYS, Inc., November 2013. [Online]. Available: http://www.ansys.com. [Accessed November 2013].

List of Table Captions

Table 3: Summary of water inlet and outlet temperature at 1C and 2C discharge rates and different boundary conditions

List of Figure Captions

Tables

Table 1 : $LiFePO_4$- 20Ah Lithium-ion pouch cell specifications

Specifications	Value
Cathode Material	$LiFePO_4$
Anode Material	Graphite
Electrolyte	Carbonate based
Nominal Capacity	20.0 Ah
Nominal Voltage	3.3 V
Dimensions	7.25 mm x 160 mm x 227 mm

Table 2 : Experimental plan

Cooling Type	Boundary Condition [°C]	Charge Rate	Discharge Rate
Water cooling	5	1C	1C, 2C
	15	1C	1C, 2C
	25	1C	1C, 2C

Table 3 : Summary of water inlet and outlet temperature at 1C and 2C discharge rates and different boundary conditions

Cooling Type	Boundary Condition [°C]	Water inlet and outlet temperature [K]			
		1C		2C	
		Inlet	Outlet	Inlet	Outlet
Water cooling	5	278.15	280.94	278.15	281.55
	15	288.42	289.33	288.42	289.93
	25	297.45	298.45	298.15	299.22

Figures

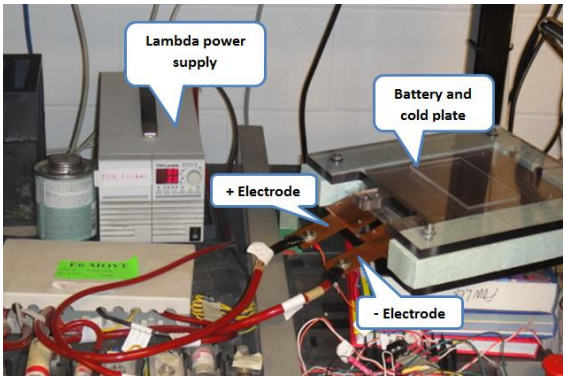

(a) Water cooling set-up

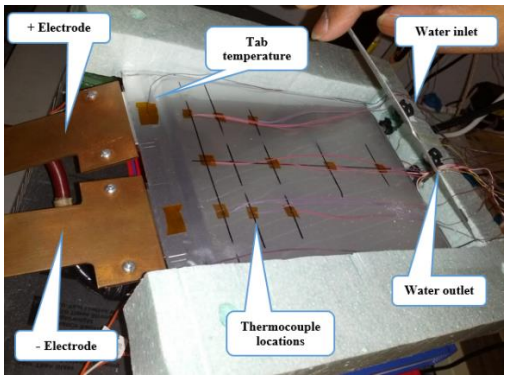

(b) Thermocouple locations

Figure 1 : Experimental set-up

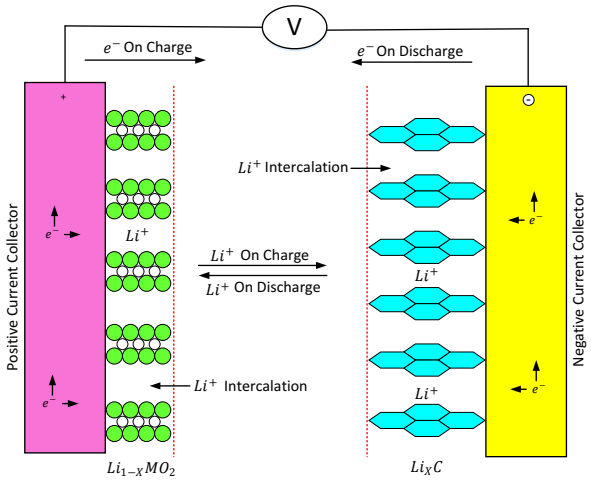

Figure 2 : Charge and discharge mechanism in Lithium-ion battery

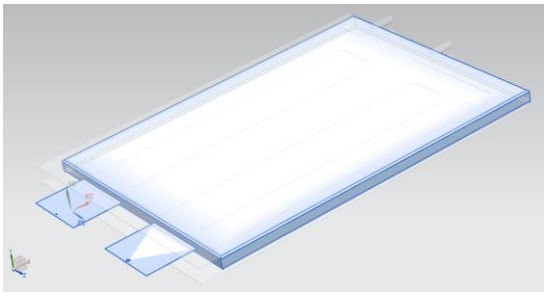

(a) Battery

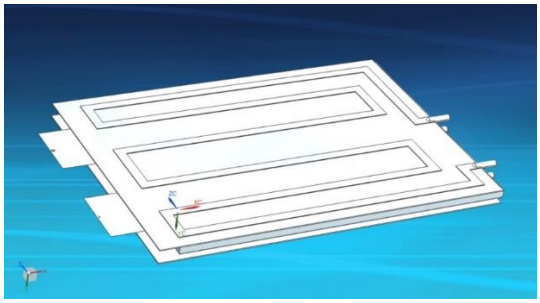

(b) Cold plate with battery

Figure 3 : Top and bottom cold plate with Lithium-ion battery in NX 8.5

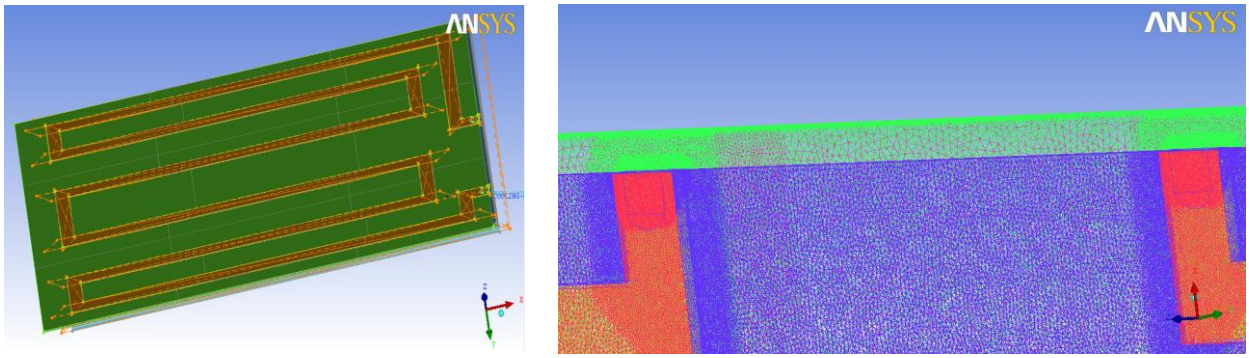

(a) Channels in cold plate **(b) enlarged portion of meshing at inlet and outlet**

Figure 4 : Inlet and outlet channel with meshing of cold plate model in ICEM-CFD

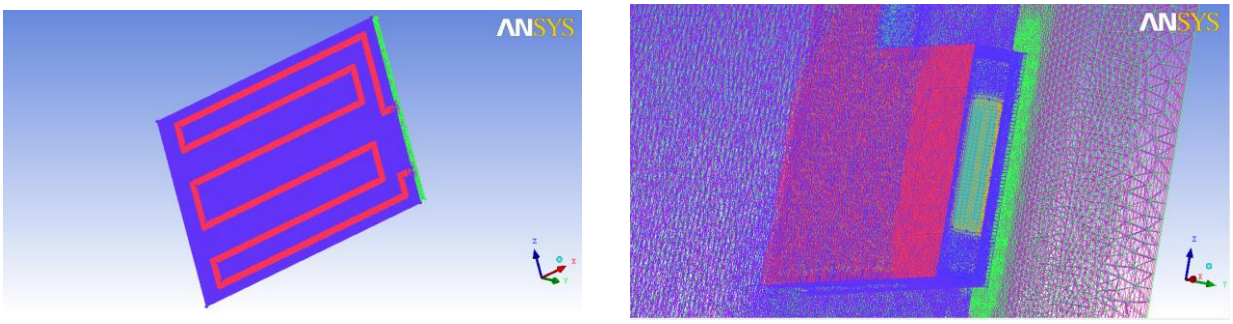

(a) Overall meshing in cold plate **(b) meshing in small portion of channel**

Figure 5 : Meshing in ICEM-CFD

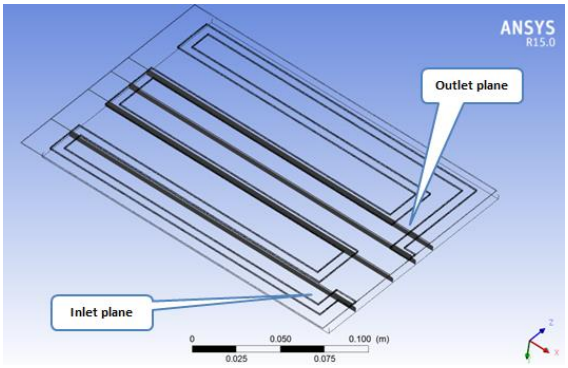

Figure 6 : Vertical planes 1, 2 3, and 4 (1 is inlet and 4 is outlet) within mini-channel cold plates

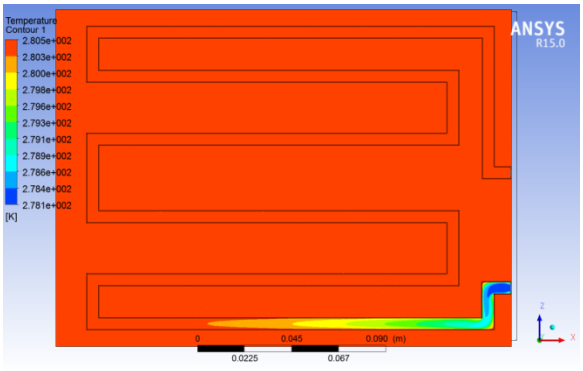

(a) Temperature contour at 1C & 5 °C

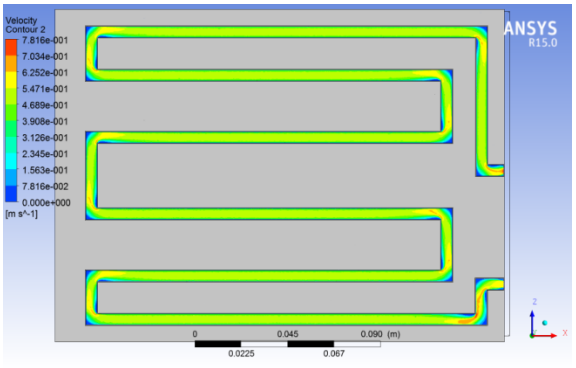

(d) Velocity contour at 1C & 5 °C

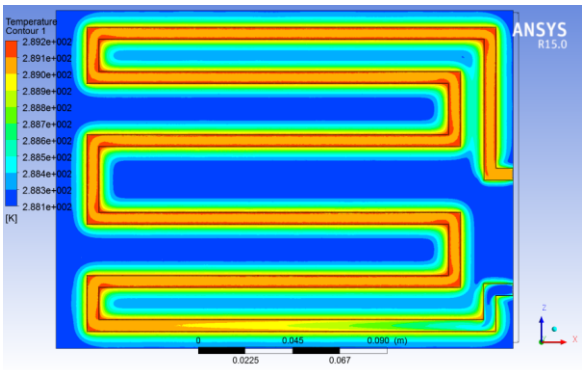

(b) Temperature contour at 1C & 15 °C

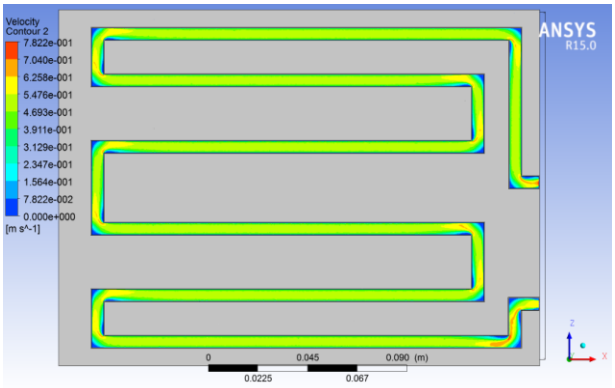

(e) Velocity contour at 1C & 15 °C

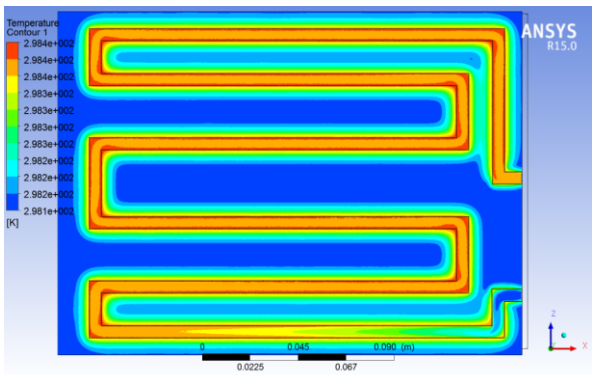

(c) Temperature contour at 1C & 25 °C

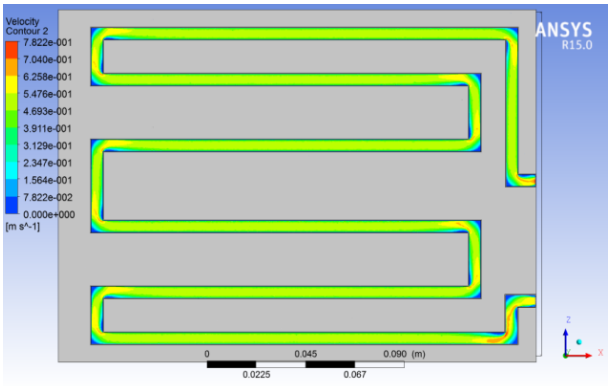

(f) Velocity contour at 1C & 25 °C

Figure 7 : Temperature and velocity contours at 1C discharge rate and 5 °C, 15 °C, and 25 °C operating temperature

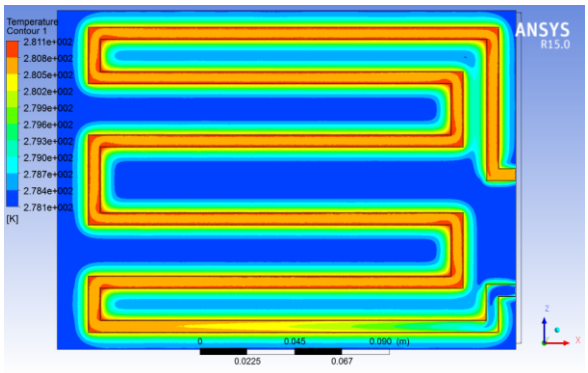

(a) Temperature contour at 2C & 5 °C

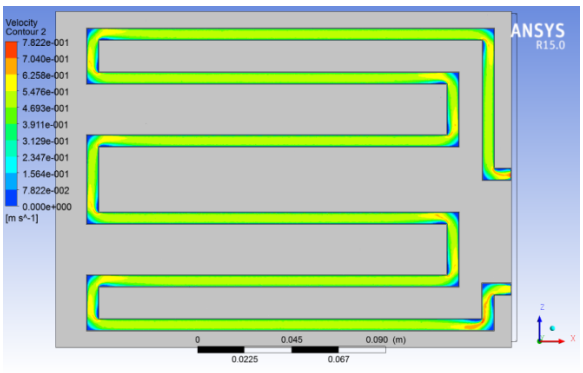

(d) Velocity contour at 2C & 5 °C

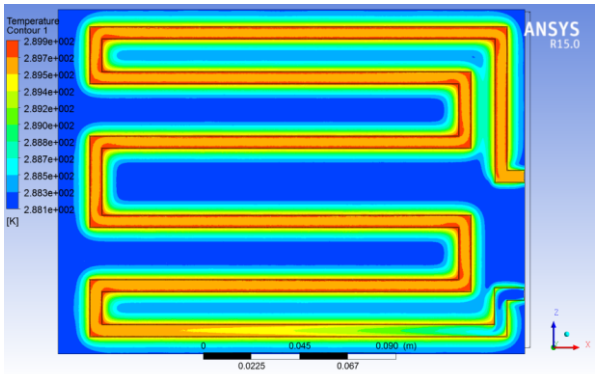

(b) Temperature contour at 2C & 15 °C

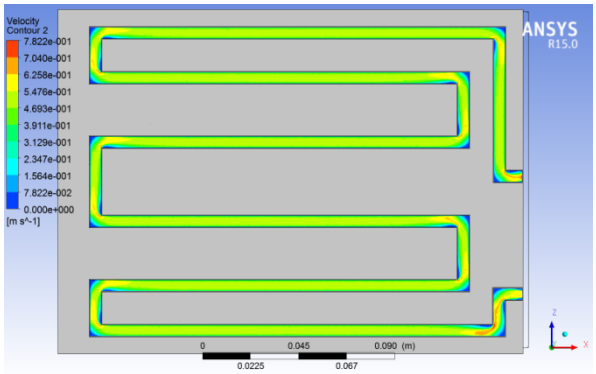

(e) Velocity contour at 2C & 15 °C

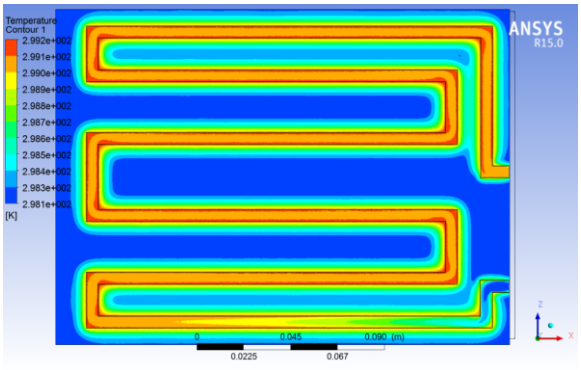

(c) Temperature contour at 2C & 25 °C

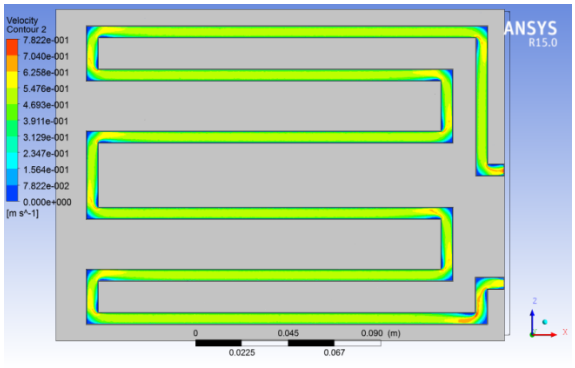

(f) Velocity contour at 2C & 25 °C

Figure 8 : Temperature and velocity contours at 2C discharge rate and 5 °C, 15 °C, and 25 °C operating temperature

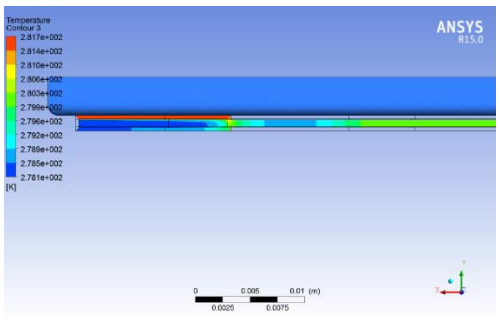

(a) Temperature contour at inlet plane 1 for 2C & 5°C

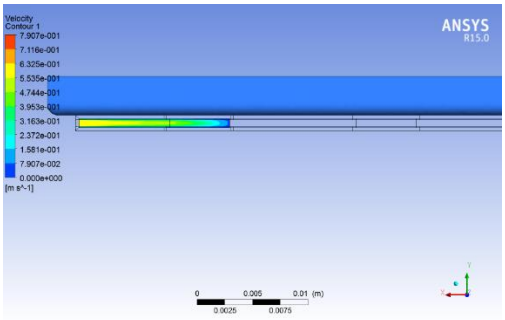

(c) Velocity contour at inlet plane 1 for 2C & 5°C

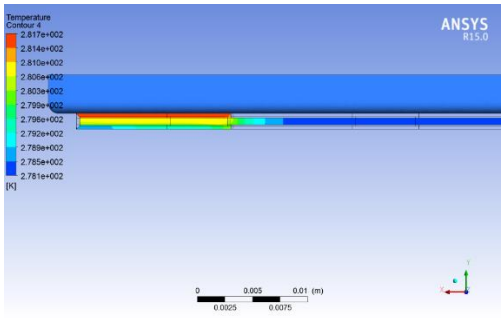

(b) Temperature contour at outlet plane 4 for 2C & 5°C

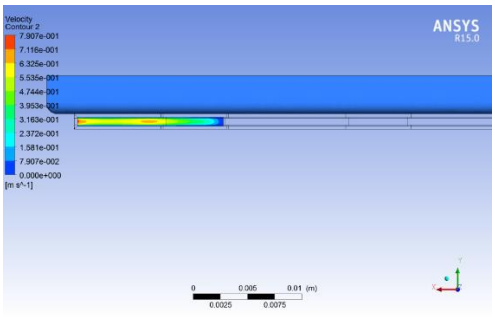

(d) Velocity contour at outlet plane 4 for 2C & 5°C

Figure 9: Temperature and velocity contours at inlet and outlet planes at 2C discharge rate and 5°C operating temperature.

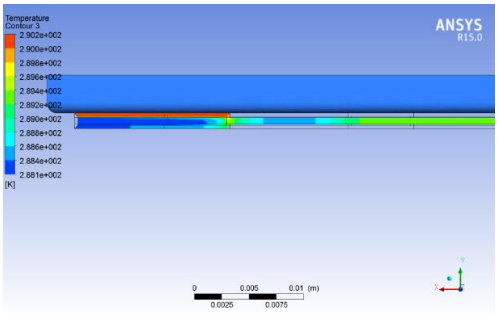

(a) Temperature contour at inlet plane 1 for 2C & 15°C

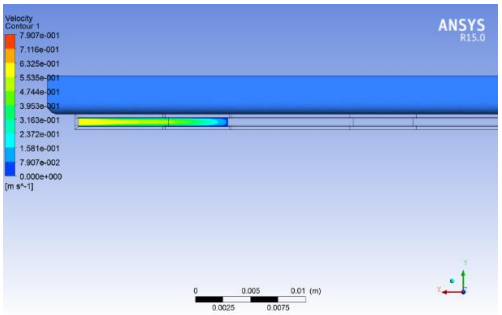

(c) Velocity contour at inlet plane 1 for 2C & 15°C

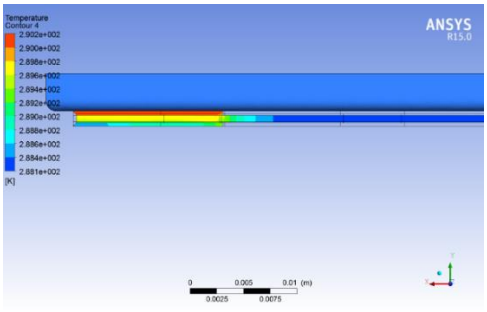

(b) Temperature contour at outlet plane 4 for 2C & 15°C

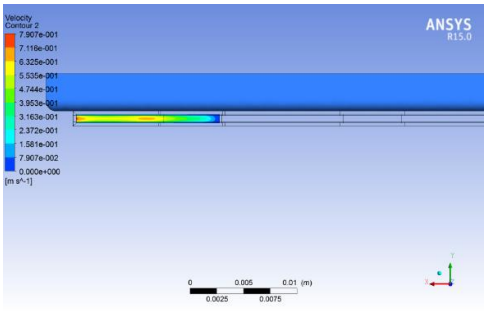

(d) Velocity contour at outlet plane 4 for 2C & 15°C

Figure 10: Temperature and velocity contours at inlet and outlet planes at 2C discharge rate and 15°C operating temperature.

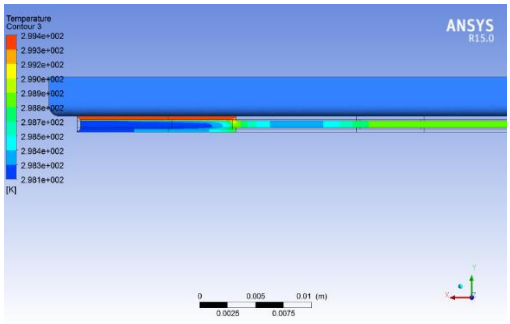

(a) Temperature contour at inlet plane 1 for 2C & 25°C

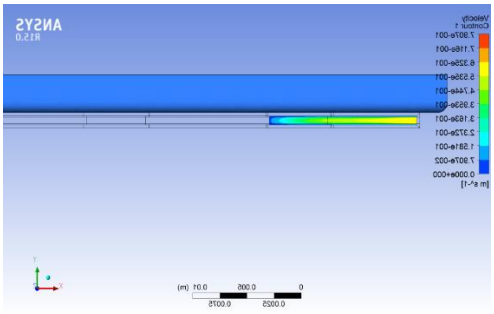

(c) Velocity contour at inlet plane 1 for 2C & 25°C

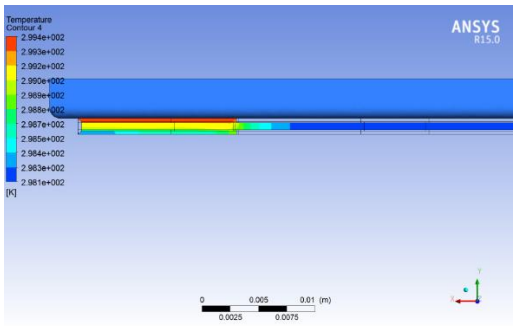

(b) Temperature contour at outlet plane 4 for 2C & 25°C

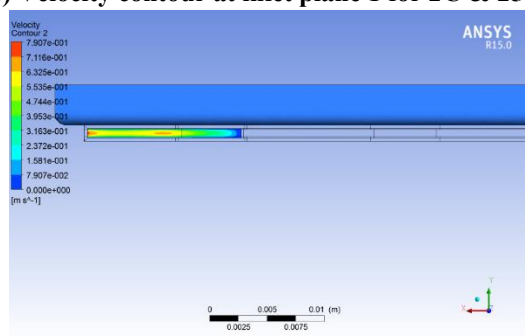

(d) Velocity contour at outlet plane 4 for 2C & 25°C

Figure 11: Temperature and velocity contours at inlet and outlet planes at 2C discharge rate and 25°C operating temperature.